ELSEVIER

ISA Transactions 35 (1996) 105–119

ISA
TRANSACTIONS®

Modeling and MIMO controller design of dense powder fluidized beds

D.E. Ventzas *

Control & Instrument Eng. Professor of TEI Lamia, Electronics Dept, Lamia, Greece

Abstract

A powder feeder consisting of a fluidized bed rig, transfer nozzle and conveyor, used in plasma spraying industry, is modeled and the system's transfer function and the MIMO closed loop control response and controller model are derived. Theoretical modeling is simulated to describe the partial and overall fluidized bed response. Copyright © 1996 Elsevier Science Ltd.

Keywords: Fluidized bed; Plasma; Nozzle; Dust feeder; Controller design; SISO, MIMO, System model and controller identification; Step response

1. Introduction

The fluidized bed is a system that transforms normal dust from the solid phase to a fluid-like phase [1]. The fluidized bed is used for [2]:

1. powder transportation,
2. spraying applications and powder ejection/injection,
3. cooling (and heat transfer) with powder,
4. material toughening and metal surface processing and finishing,
5. packaging, etc.

Its applications are in the area of powder technology [3], i.e. in

1. the pharmaceutical industry,
2. the glass industry,
3. alumina powder,
4. coal burners.

The paper studies a fluidized bed process, its powder feeder and conveyor and a novel electrostatic type of flow sensors; it models the sensing mechanism, the sensing and actuating elements and designs a sufficient SISO and MIMO controller for the system.

Arrangements of *single or array nozzles* give efficient fluidized powder stream performance with good spraying and coating quality.

Temperature conditions could reach 18,000°K in plasma torches [4].

Reliable instrumentation and control of fluidized beds and dust feeders is a basic demand of modern industry [5]. The powder mass flow process model and control are investigated here.

2. The rig

The fluidized bed, see Fig. 1, consists of:

1. a *powder storage–agitation* section (transparent perspex),

* Correspondence address: Analipseos 124, Volos 382 21, Greece.

PII S0019-0578(96)00013-4

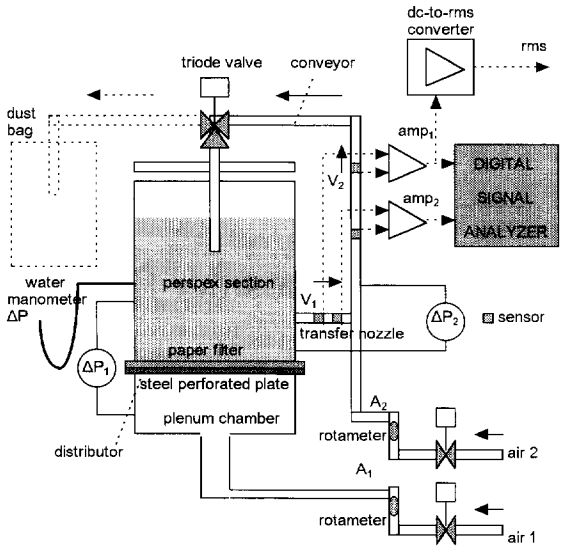

Fig. 1. Fluidized bed.

2. a filter of thick paper or cloth to avoid powder back-flow,
3. a perforated steel plate allowing air to agitate the powder.

A *transfer nozzle* and the adjoining *conveyor* complete the rig.

The fluidized bed described here, delivers *accurate* known *quantities of solids* by air. Phase collapse, air flow blockages and non-uniform flow rates caused by powder suggest that the *dust feeder* is the most sensitive part of the rig, see later.

The plasma operating conditions dictate that the important parameters (i.e. input, control, output parameters) affecting the spraying efficiency are [6]:

h = height of fluidized bed,

V_1 = velocity of solids in the transfer nozzle (which is linearly dependent on the mass flow rate entering the plasma gun),

V_2 = velocity of conveyed solid in the feed pipe (arc gas flow rate $> 4 \times$ powder gas flow rate),

A_1 = air flow rate passing into the bed's plenum chamber; it controls the mass flow rate entering the conveyor,

A_2 = air flow rate carrying the solid through the pipe; it determines the powder's velocity in the conveyor,

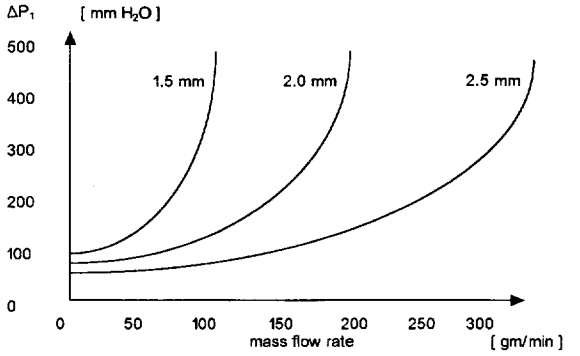

Fig. 2. Bed pressure drop, ΔP_1, versus nozzle outflowing mass flow rate characteristics (for steel nozzles 25 mm long $\times$ indicated diameter).

ΔP_1 = fluidized bed's filter pressure drop (supports the bed), see Fig. 2,

ΔP_2 = pressure drop of nozzle, see Fig. 3,

W = powder loading (total powder mass circulated in the bed),

The fluidized bed pneumatic–conveyor system specifications are given in Table 1.

In a fluidized bed, see Fig. 1, air flow causes a pressure drop, ΔP_1, across the paper filter and the perforated steel plate, which, if it is sufficient, *supports the weight of the bed's powder particles.* A flow increase causes the bed to expand to accommodate the volume increase; the fluidized bed's height

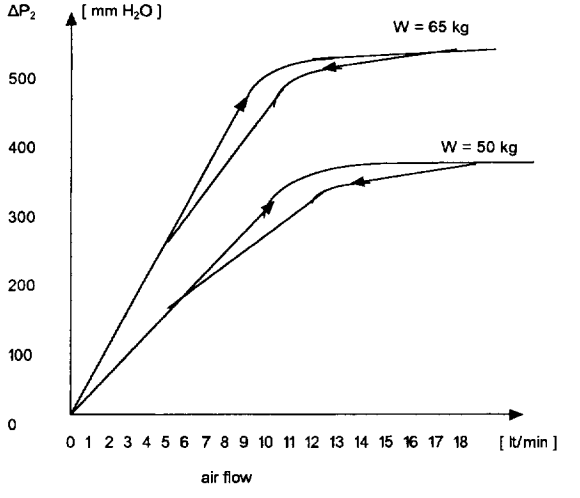

Fig. 3. Fluidized bed characteristic.

Table 1
Fluidized bed rig specifications

Pipe diameters	4–12 mm
Loading	10–100 gm/min
Loading accuracy	±5%
Powder gas flow	4–7 lt/min
Velocities	4.5–9.0 m/s
Loading solids-to-air ratio	22:1
ΔP	0–600 mm H_2O
A_1	0–37 cfh
A_2	8–15 cfh
W	30–70 kg
Phases	2 (air, powder)
Particle size	60 μm
Particle shape	spherical
Intrinsic safety	NO

(level) is a critical parameter considered throughout the experiments. A *hysteresis* is observed, see Fig. 4, that depends on the degree of consolidation in the original bed; going down the slope B the particles are more loosely packed and consequently the bed level is higher and ΔP_1 smaller [7].

The pressure drop across the bed forcing the powder through the nozzle must be greater than the pressure drop across the mouth of the nozzle at the conveyor junction, i.e. $\Delta P_1 > \Delta P_2$, otherwise flow through the nozzle will cease. In order to reduce the pressure through the conveyor system it is necessary to:

1. use a larger pipe diameter,
2. use a venturi ejector,
3. apply smaller air flow rates,
4. locate the exit nozzle near the end of the conveyor line.

An increment of the pressure head at the nozzle overcomes back-pressure, but small nozzle diameters are susceptible to blockages, so their mechanical and aerodynamic designs are critical.

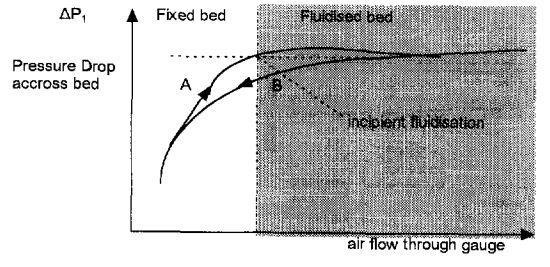

Fig. 4. Non-linear characteristics of a fluidized bed.

The dust filter in the base of the fluidized bed is made from *material* that depends on the circulated dust and the carrying velocities. The same holds for the dust collecting bag at the other end of the conveyor. Dust collection can be achieved by different collecting techniques, such as pulse jet, reverse air, shaker collector and cyclones with varying collecting efficiency [8].

3. The computerized flow measurement system model

An 8-bit microcomputer implements the flowmetering and control signal processing algorithms, see Fig. 5. An indirect mass flow rate technique is used, see later. The interface is a standard n^* dual channel ADC with its timing and peripheral interface adaptor circuitry. Microprocessor measurement includes: data capture (batch or real time), correlation analysis and peak searching and finally display; it supports the measuring system, the process control, the mass flow measurement and the system's general housekeeping, i.e. it is a stand-alone intelligent *industrial sensor-controller*.

The principle of *cross-correlation flowmetering* is the following: For two flow signals $x(t)$, $y(t)$ (in the case of electrostatic transducers corresponding to an electrostatic signal) generated at distance L apart downstream and sensed by two (electrostatic) sensors we get the cross-correlation function:

$$R_{xy}(\tau) = \int_0^T x(t)^* \, y(t+\tau) \cdot d\tau.$$

The cross-correlation function $R_{xy}(\tau)$ is *maximized* for time delay τ^*, where:

$$\tau^* \propto \frac{L}{v}$$

where v is the fluid velocity [9].

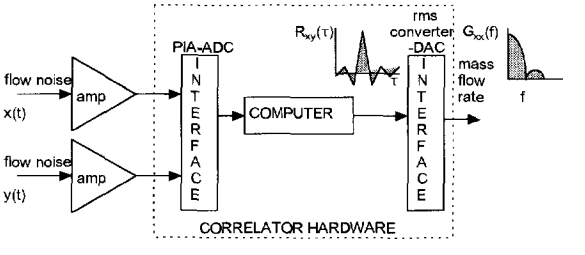

Fig. 5. Measurement system block diagram.

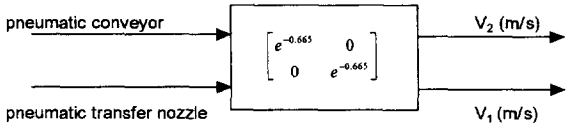

Fig. 6. Measuring system transfer function.

The laboratory computer, used in the experiments, implements concurrently:

- system model output,
- direct digital control (DDC) and process control algorithm,
- signal processing,
- flow velocity measurement and mass flow measurement.

For the SISO case one correlation flowmeter is used, while for the MIMO case two correlation flowmeters are needed. The author has developed [10,11] a 4 channel × 1 bit correlator and a 2 channel × 4 bit correlator for such applications. Computer controlled multiplexing techniques further increase process signals management and measuring flexibility.

The measuring system consists of:

1. an amplifier (FET, opamp),
2. an interface,
3. a mass flow rate indicator.

The amplifiers response time is 10^{-6} sec, i.e. much faster than the process dynamics. The measurement rate is:

$T_m = T_L + T_p$, i.e.

Total Measurement Time = Data Logging Time + Data Processing Time.

This will appear as a pure time delay whose value depends on:

- process signal bandwidth,
- flowmeter clock period,
- integration time and function mode.

A typical transit time for our correlation flowmeters is 0.665 sec.

The flowmeter model for our fluidized bed consists of two independent (i.e. decoupled) flowmeters with the transfer function given in Fig. 6.

4. The sensors

The sensing system consists of metallic plates insulated from a perfectly grounded pipe wall and shielded against electrical interferences. It operates by induction since the particles are pneumatically conveyed charged powder and generate varying electric fields on the sensors [12]. Signal conditioning is achieved by high impedance amplifiers.

Different sensor geometries and installations were tested, see Fig. 7. The sensor types are:

1. externally mounted plate,
2. coils,
3. externally mounted rings,
4. exposed rings or plates.

Externally mounted ring sensors of 1 cm^2 area were the preferred type because they are:

1. fast, reliable, continuously operated,
2. non-intrusive,
3. independent of the gas powder state,
4. non-energy consuming,
5. maintenance free.

The sensors sense charged particles and dipoles by electrostatic and electromagnetic induction mechanisms [13]. The polarity of the charges depend on the (powder and pipe) materials position in the triboelectric series and Lenz's law [14]. For example, alumina powder is charged positively; the type of electric field characteristic, i.e. rms voltage level with probe–source distance is given, in Fig. 8.

Powder recycling tends to charge pure uncharged powder, thus driving the electrostatic sensor to saturation and insensitivity [15]. This means that the measuring system is an over sensitive device, depending on physical state of the fluidized bed, i.e.:

1. particle size and shape,
2. nature and charged state of powder
3. nature and surface of pipe wall.

The accumulated charge, V_{dc}, over a plastic pipe increases with conveyor length downstream, reach-

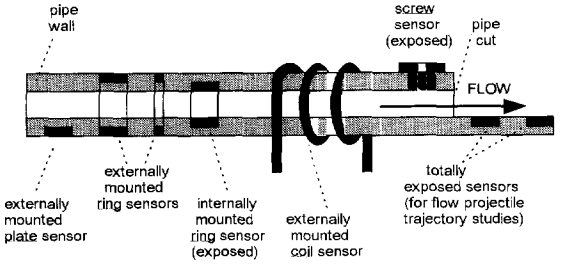

Fig. 7. Sensor geometries.

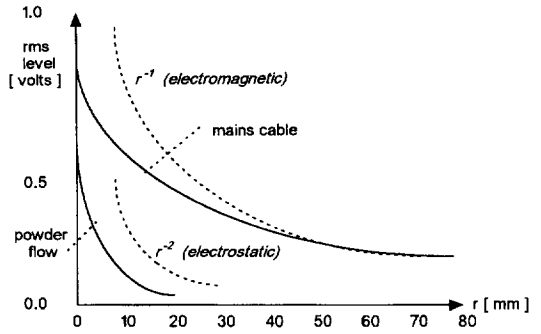

Fig. 8. Type of electric field characteristics.

ing a maximum at its end; this is minimized by pipe screening and/or grounding [16].

Increment of powder mass flow increases the rms level of the induced flow noise, see Fig. 9; this is very important for mass flow measurement. Increment of sensor dimensions (pick-up area) low pass filters the flow noise, see Figs. 10–12 and Table 2.

Dual electrodes distance experimentation (upstream-to-downstream sensor) for cross-correlation implementation suggests minimal sensor distances, i.e. 1 cm; this is logical, since high frequency components result in sharper correlograms, which define *accurate transit time delays*; high frequency induced flow noise is highly attenuated downstream, resulting in uncorrelated high frequency components, i.e. the low frequency flow noise dominates, resulting in flat peaked correlograms and inaccurate transit time derivation. The lower cut-off frequency is at 60 Hz, filtering the low frequency content of the flow noise

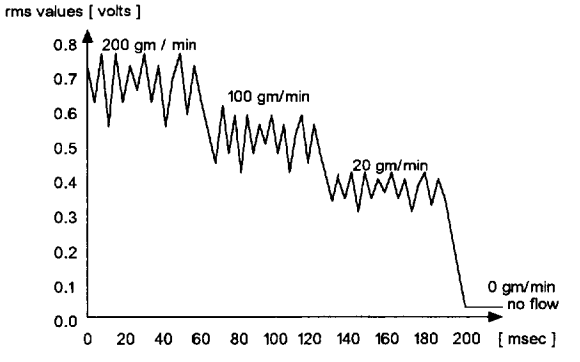

Fig. 9. Typical rms chart recording in a 10 mm pipe with exposed sensor.

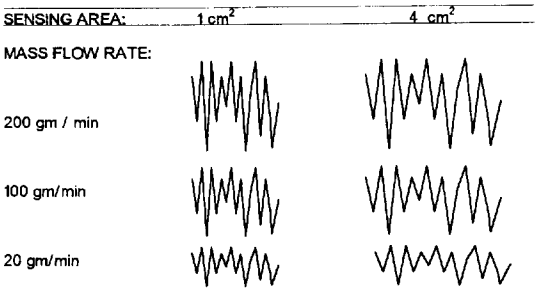

Fig. 10. Typical rms chart recording in a 10 mm pipe with short/large sensor.

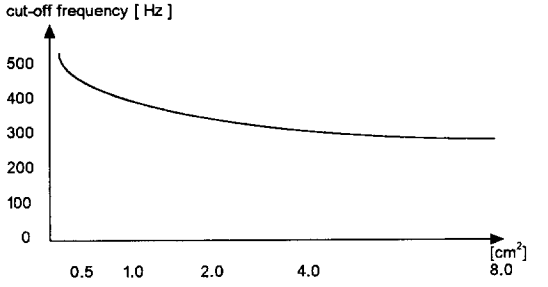

Fig. 11. Sensor bandwidth with sensor area.

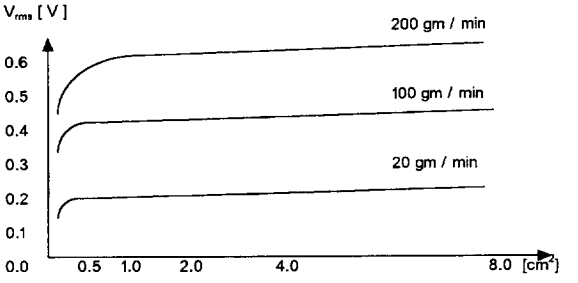

Fig. 12. Sensor sensitivity with sensor area.

Table 2
Electrode area effect on signal level and frequency cut-off frequency (Hz)

Electrode area (cm^2)	Rms volts			Cut-off frequency (Hz)
	Mean flow rate (gm/min)			
	20	100	200	
0.5	0.19	0.39	0.50	440
1.0	0.19	0.45	0.56	360
2.0	0.19	0.49	0.60	330
4.0	0.18	0.47	0.63	270
8.0	0.21	0.50	0.65	240

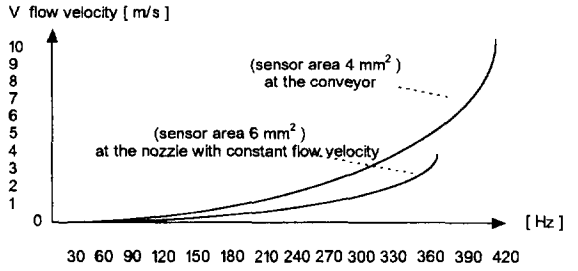

Fig. 13. Electrostatic signal bandwidth with flow velocity.

signal caused by electrostatic charge build-up and mains interference [17].

The sensors located on the conveyor have a greater bandwidth, since they are exposed to higher flow velocities, but the nozzle has greater bandwidth for the same velocity, since its electrode area is smaller, see Fig. 13. In conclusion, we might say that:

1. probe area is inversely proportional to flow noise bandwidth,
2. probe area is proportional to rms level of flow noise,
3. rms of flow noise is sensitive to mass flow rate for steady powder velocity,
4. bandwidth of flow noise is independent of mass flow rate for given sensor and for steady powder velocity.

The transfer function model relating the turbulence of the conveying fluid to changes in the electrode's static electricity due to the conveyed phase depends on the inertia of the conveyed phase, viscous drag between conveyed and conveying media, gravitational forces and the spatial filtering effects caused by the electrode's geometry, see Fig. 14.

Our model is based on the net number of particles passed through a cross-section of the pipe; the model is better suited to light phase powder flows, where the interparticle interactions are weak; excessive particle flow leads to saturation effects on the electrodynamic transducer. The detected flow noise is a result

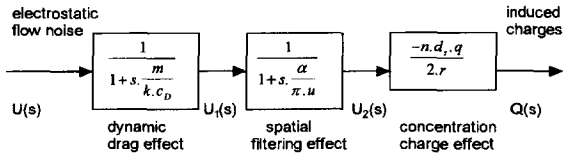

Fig. 14. Turbulent two-phase model block diagram.

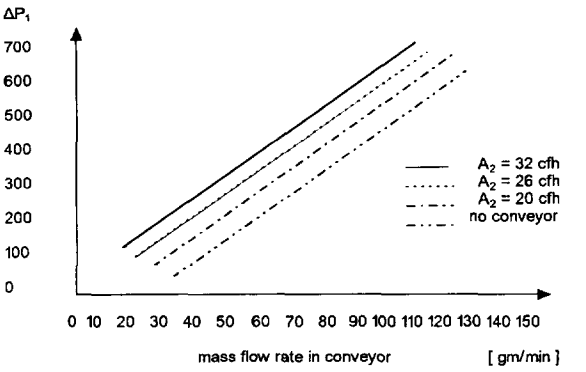

Fig. 15. Mass flow rate calibration curves of plasma spraying (30 mm * 1/8" transfer nozzle – 1/4" conveyor).

of the product of the actual flow noise and the transducers transfer functions.

5. Electrostatic flow noise rms-to-mass flow rate correlation

The described measuring device calculates the mass flow rate by calculating the powder velocity, selecting the appropriate rms value — mass flow rate curve, see Figs. 15 and 16, and finally interpreting the actual mass flow rate; the measuring system output is either an analogue voltage or a 4–20 mA current loop.

Experimental tests of the principles and feasibility of the *electrostatic induction transducer* as a powder flowmeter covers:

1. elucidating mechanisms of charge generation and detection [18],

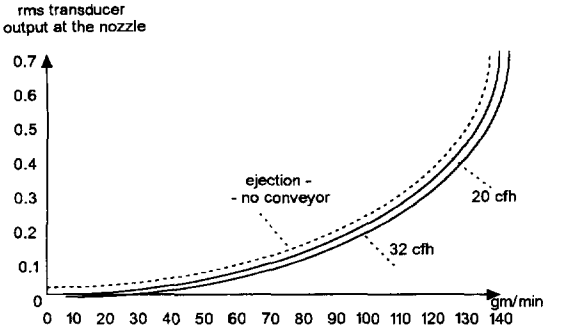

Fig. 16. Nozzle transducer response as an rms mass flowmeter.

2. probe geometry, electric properties, location effects on signal response,
3. cross-correlation accuracy in flow velocity calculations,
4. transducer tests on very dense, dense and lean flows,
5. rig operation (velocities, powder concentration, humidity, temperature),
6. powder nature and electrical properties.

Researchers [19] suggested other exotic mechanisms of electrostatic charge generation such as electrolytic, spray and aerosol electrification, homogeneous charge generation, gas–ion surface exchange, thermionic emission, and photoelectric effects and actions. Direct current (dc) charges are due to charge build-up and they are susceptible to drift, while we are interested in *ac components*, corresponding to the actual powder flow properties; we suppose that electrostatic charges are highly coupled to the mass flow, a reasonable assumption. Alternative charge current components are enhanced by charging mechanisms and attenuated by dipoles, these accumulation and discharge mechanisms result in a random nature, or at least a pseudorandom one.

For ring sensors the rms value can be used as a crude mass flowmeter, see Fig. 16. At higher carrier gas flow rates the transducer responds in a way independent from pipe orientation (vertical, horizontal, angled); this is due to leaner phase condition.

The rms value of the electrostatic charge flow noise leads to $\pm 5\%$ random errors of mass flow measurement, a theoretical limit for the most of the correlation flowmeters.

The rms (root mean square) value of the ac flow noise, $x(t)$, is:

$$x_{rms}(t) = \sqrt{\lim_{T\to\infty} \frac{1}{T}\int_0^T x^2(t)\cdot \mathrm{d}t}.$$

For an ergodic process:

$$x_{rms}(t) = \lim_{f\to\infty}\int_0^f G_x(f)\cdot \mathrm{d}f = \lim_{f\to\infty}\sigma^2 = R_x(0)$$

where,

$R_x(0)$ = the autocorrelation of $x(t)$ at $\tau = 0$, i.e. zero time displacement,
$G_x(f)$ = the power spectrum of $x(t)$,
σ = total noise power in the flow signals,
W = powder loading.

The flow noise is almost Gaussian, with spectrum $G_x(f)$ and a cut-off frequency f_c, that increases in proportion to the number of particle collisions [20]:

$$f_c \propto N \Rightarrow f_c \propto W.$$

The total noise power in the flow signals σ, depends on the number of particles:

$$\sigma \propto N \Rightarrow \sigma^2 \propto W^2$$

$$\sigma^2 = \int_0^\infty G_x(f)\cdot \mathrm{d}f$$

$$\Rightarrow \sigma^2 = f_c \cdot G_x(f),\ \sigma^2 \propto W^* G_x(f).$$

The above relations suggest that:

$$W \propto G_x(f).$$

The observed power spectrum is the convolution between the $G_x(f)$ and the sensors transfer function $k\cdot G(s)$, i.e.:

$$G_m(f) = G_x(f)^* k\cdot G(s)$$

and finally:

$$W \propto \int_0^f G_m(f)\cdot \mathrm{d}f = x_{rms}^2.$$

The rms value of $x(t)$ is proportional to the power content, and it can be reasonably suspected to be in some way proportional to the powder mass flow rate. The number of equally sized particles N around the electrode is proportional to the loading W and the mean square value (x_{rms}^2):

$$N \propto W \propto x_{rms}^2 \Rightarrow x_{rms} \propto \sqrt{W}$$

For an isolated brass pipe with solids loading ratios ≤ 3, Baum et al. [15] suggested that the current measured is:

$$i = \frac{Ms}{\frac{\pi}{6}\cdot D_p^3\cdot \rho_p}\cdot k\cdot (q_1 - q_0)\cdot (1 - \mathrm{e}^{-k\cdot n})$$

where:

M_s = solids loading,
D_p = particle diameter,
ρ_p = particle density,
q_0 = initial charge on particle,
q_1 = final charge on particle,
n = number of collisions.

Others [21] suggested that the current generated by particle collisions on a cylindrical probe is:

$$i = \frac{\left(R \cdot \frac{\pi}{2} \cdot N \cdot r \cdot l \cdot \bar{v} \cdot q_p\right)}{V_p}$$

where,

R = the ratio of collision cross-sectional area to projected area of probe normal to the flow direction,
V_p = the particle velocity,
N = density number,
r = radius of probe,
l = length of probe,
q_p = charge transferred at each impact,
$\bar{v}$ = particle velocity hitting wall due to random motion.

The rms conversion is possible by software, approximated by $R_x(0)$ or by hardware; the AD536A IC is an rms-to-dc converter, giving:

$$V = \left[\frac{V_{in}^2}{V_{rms}}\right]$$

for a resulting rms output signal bandwidth of 30 Hz.

The experimental results, see Fig. 16, show a good agreement between rms and the square root of the mass flow rate; the proportionality constant depends on powder velocity and humidity; maintaining the rate of charging at standard conditions increases the cost of the process. Excessive particle population results in saturation effects on the sensors, resulting in severely band limited flow noise, where the Gaussian statistics no longer prevail.

6. Calibration

Independent powder flow measurement methods are used for velocity and mass calibration purposes; two such methods are:

1. powder *flow projectile trajectory method*, ruled by the following parameters:

(i) bed height,

(ii) powder, free stream (no conveyor), velocity $= \sqrt{(g \cdot x^2)/2 \cdot y)}$

(where x and y are the powder jet free stream coordinates), or alternatively:

2. the classical *weighing method.*

The projectile method is a dynamic one, while the weighing method although static is objective.

A parallel criterion suggesting high flowmeter accuracy is the maximum *cross-correlation coefficient persistence*, i.e. for a steady flow correlogram resistant to noise corruption and even temporary collapse; typical correlation coefficients values vary around 0.69. Correlogram inconsistencies result either from flow changes or sensing method nonlinearities or both; this introduces further problems in the measuring method. Large integration times overcome these problems, but the measurement and control becomes insensitive to flow changes.

Vertically positioned conveyors assure no sensor powder accumulation, i.e. electrostatic charge build-up, but the fluid is exposed to *gravitational forces.* Flexible conveyor deformation or movement results in *pressure fluctuations* in the line and phase separation, which causes the powder to settle on the pipe irregularities (low pressure points).

7. The powder feeder

The powder feeder is the most sensitive part of the fluidized bed rig. It is capable of mixing gas with powder in a specific ratio and conveying it (under pressure control) along a feed line. Commercial dust feeders include a powder hopper [22,23]. It is preferable to vary the powder feed rate at a given carrier gas supply, without altering other settings.

The dust feeders available are of different types:

1. rotating paddle feeder (that results in pulsating flows),
2. venturi aspirating feeder (with blockage problems),
3. screw feeder (that wears quickly with abrasive powders),
4. logarithmic spiral collector (limited to high 15 lt/min air flows),
5. inverted cone (collecting dust by swirling around the cone); this is the most popular, due to simplicity, see Fig. 17

In low flows the solids density within a transfer nozzle decreases from 0.5 gm/cm^3 to 0.2 gm/cm^3; this is caused by the pure aerodynamic design of the nozzle, i.e. the back-up pressure and flow, that causes

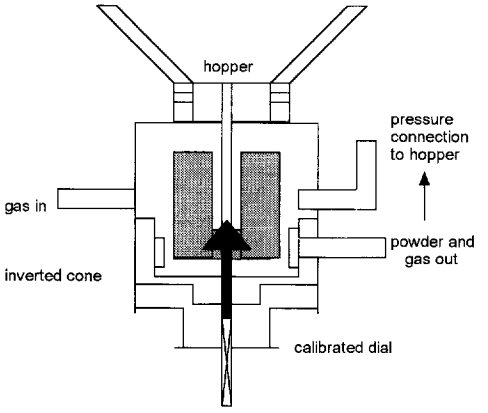

Fig. 17. Inverted cone dust feeder.

less powder to flow through the nozzle. Nevertheless, the method monitors all powders exhibiting triboelectric properties.

The powder density in the bed is:

$$p_b = \frac{bed\,mass}{bed\,volume} = 0.80\ gm/cm^3.$$

The powder density in the nozzle is:

$$p_n = \frac{mass\,collected}{velocity \cdot orifice\,area} = 0.60\ gm/cm^3,$$

i.e. it is believed that the powder density in the nozzle is slightly lower than the powder density in the bed.

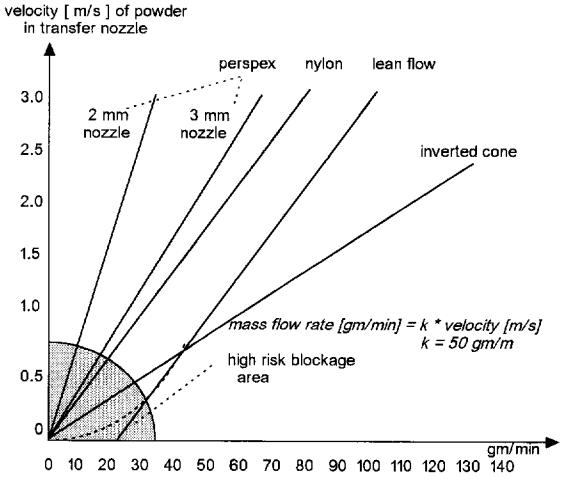

Fig. 18. Flow density characteristic of dust feeder.

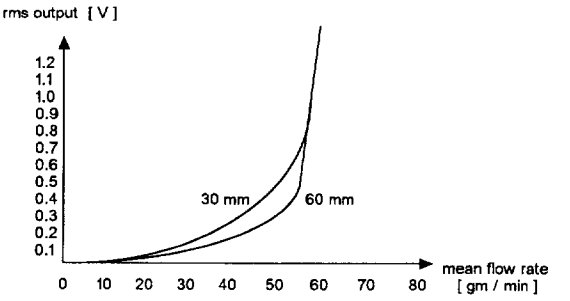

Fig. 19. Transducer rms output for nylon nozzles.

Perspex and nylon nozzles, although they tend to saturate, are very sensitive to electrostatic flow noise and flow changes (nylon is more sensitive than perspex), see Fig. 18. It is believed that since perspex and nylon have similar dielectric constants and work functions, their surface's nature and uniformity has a significant effect on the *rate of charging*; nylon nozzles have smoother bores than perspex ones. Nozzle *sensitivity* results in higher bandwidth flow signals and quicker flowmeter response.

Although perspex nozzles present rms output vs. mean flow rate inconsistency, nylon ones are very promising, see Fig. 19.

8. Dust feeder model

The fluidized bed dust feeder is basically a 2 input/2 output device, with process input variables:

A_1 = air flow rate passing into the bed's plenum chamber

A_2 = air flow rate carrying the solids through the pipe.

A_2 will directly influence V_1, the velocity of the solids in the transfer nozzle (which is linearly dependent on the mass flow rate) and V_2, the velocity of

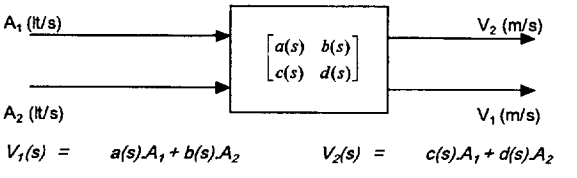

Fig. 20. Plant transfer function block diagram.

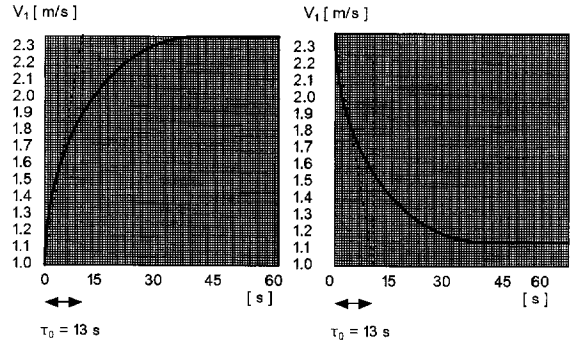

Fig. 21. Step response to calculate $a(s)$ ($A_1 = 2$–5 lt/min $\approx$ 56–114 gm/min, $A_2 = 26$ cfh).

the conveyed solids in the feed pipe. Some interaction occurs between inputs and outputs, see Fig. 20.

An open loop transfer analysis on each subsystem is carried out using classical identification techniques. A step disturbance on each input (maintaining all others constant) interrogates the system, producing on all process output the system step response.

The process is interrogated over the typical plasma operating conditions (0–100 gm/min at 20–32 cfh). The open loop step responses for the process (dust feeder) are given in Figs. 21–24.

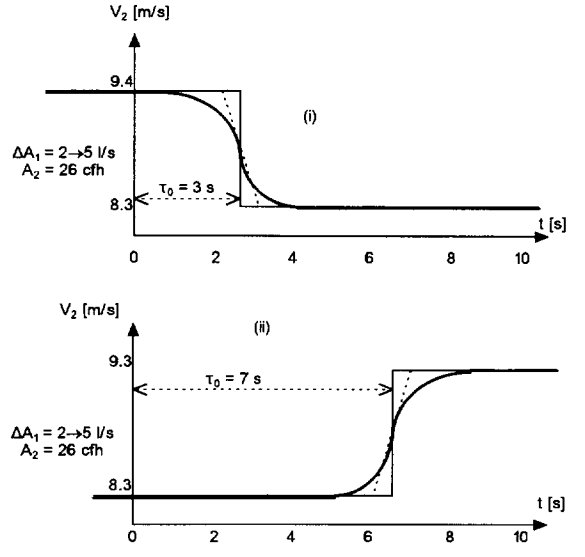

Fig. 22. Step responses to calculate $c(s)$.

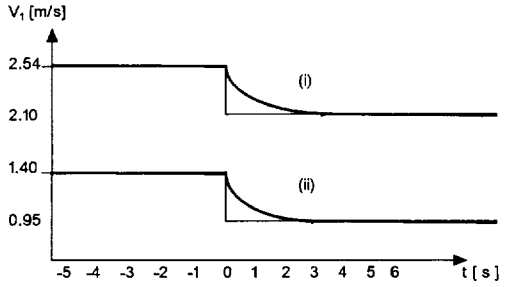

Fig. 23. Step responses to calculate $b(s)$ ($A_1 = 2$–5 lt/min, $A_2 = 20$–32 cfh).

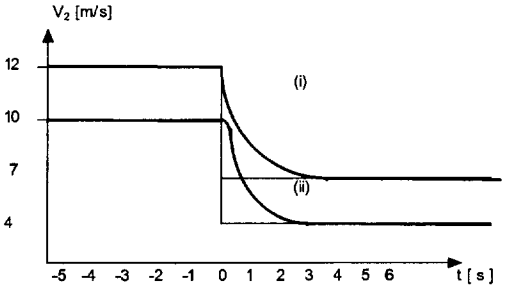

Fig. 24. Step responses to calculate $d(s)$.

The above step response tests suggest that:

$$a(s) = \frac{10.6 * e^{-s}}{13 * s + 1}, \quad c(s) = 9.8 * e^{-5 * s},$$

$$b(s) = 8.2\,\text{m/lt}, \quad d(s) = 101\,\text{m/lt}.$$

9. The actuator

Electrically operated analog valves have fast response but high cost. The widely used pneumatic control valves will present a dynamic lag. The step

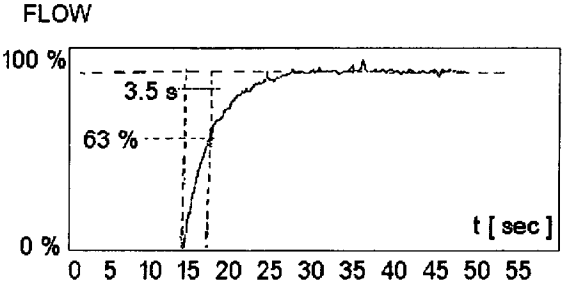

Fig. 25. Step response of pneumatic control valve.

response of a used miniature pneumatic control valve, under fluidized bed operating conditions, is given in Fig. 25.

Therefore the control valve's open loop transfer functions for the air streams A_1 and A_2 are:

$$G(s)_{V_1} = \frac{0.0150}{3.5^* s + 1}, \quad G(s)_{V_2} = \frac{0.0075}{3.5^* s + 1}.$$

The time constants are derived graphically from the step responses curves, while the valve gains are derived by the control valve sizing formula:

$$K_V\,[\mathrm{lt/s/mA}] = \frac{\textit{airflow control range}\,[\mathrm{lt/s}]}{\textit{driving current range}\,[\mathrm{mA}]}$$

The denominator is always *20 mA − 4 mA = 16 mA*.

A conventional controller output of 4–20 mA (electric) or 3–15 psi (pneumatic) is used, in association with an I/P (electric-to-pneumatic) converter.

10. SISO controller scheme

The single loop negative feedback control system with its identified transfer function is given in Fig. 26.

The mass flow rate, V_1 is investigated here, since the significance of V_2 is secondary compared to maintaining a required mass flow level. This can be achieved by using a single loop controller to regulate the most important process variable V_1.

Cohen and Coon [24] applied a small step change in the manipulated variable and recorded V_1 in time. The derived dust feeder transfer function has the form:

$$G_p(s) = \frac{K_p \cdot e^{-T_d^* s}}{\tau^* s + 1}$$

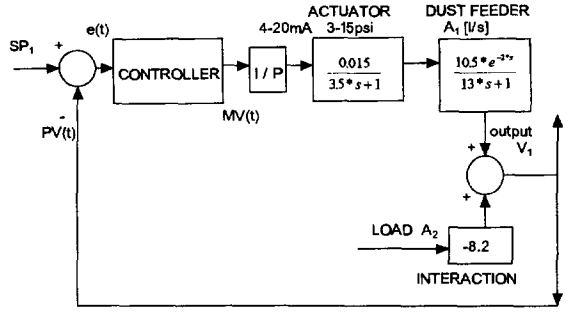

Fig. 26. SISO Control System Modeling.

where,

K_p = the process gain = 10.5,

T_d = the time delay = 2 s,

τ = the major time constant = 13 s

The load disturbance caused by changes in A_2 carrier gas stream on V_1 is shown as a negative influencing gain. The effect of fluctuations in A_2 on V_1 can be considered as load disturbances, using a gas flow indicator on the identified interaction block.

Controller tuning is performed [25] by the classical methods (i.e. minimum offset, fast response and minimal overshooting). Concluding that control valve lag compared with the process time constant is

$$\tau_v = 3.5\,\mathrm{s} < \tau$$

the following controller settings are recommended:

For pure proportional (P) control:

$$K_c = \frac{l \cdot \tau}{K_p \cdot T_d} \cdot \left(1 + \frac{T_d}{3 \cdot \tau}\right), \quad \text{i.e. } K_c = 50.1,$$

For proportional and integral (PI) control:

$$K_c = \frac{l \cdot \tau}{K_p \cdot T_d} \cdot \left(\frac{9}{10} + \frac{T_d}{12} \cdot \tau\right), \quad \text{i.e. } K_c = 43.5,$$

$$i = T_d \frac{30.3\frac{T_d}{\tau}}{9 + 20 \cdot \frac{T_d}{\tau}}, \quad \text{i.e. } i = 4\,\mathrm{s},$$

and reset time:

$$1/i = 0.25\ \mathrm{s}^{-1}.$$

For proportional, integral and derivative (PID) control:

$$K_c = \frac{l \cdot \tau}{K_p \cdot T_d} \cdot \left(\frac{4}{3} + \frac{T_d}{\tau}\right), \quad \text{i.e. } K_c = 65.3,$$

$$i = T_d \frac{32 + 6 \cdot \frac{T_d}{\tau}}{13 + 8 \cdot \frac{T_d}{\tau}}, \quad \text{i.e. } i = 4.6\,\mathrm{s},$$

and reset time:

$$1/i = 0.21\ \mathrm{s}^{-1},$$

$$D = T_d \frac{4}{11 + 2 \cdot \frac{T_d}{\tau}}, \quad \text{i.e. } D = 0.7\,\mathrm{s}.$$

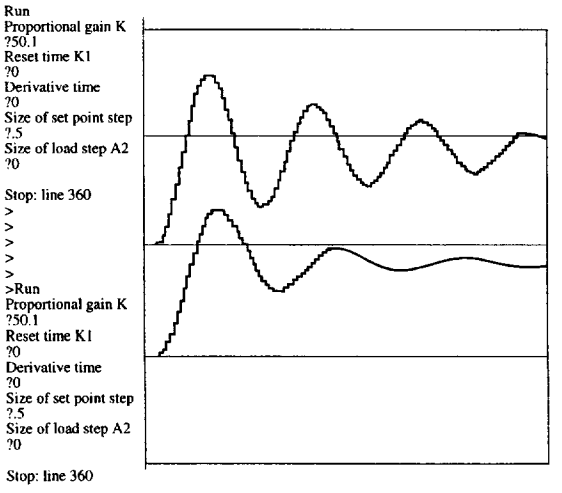

Fig. 27. P control of SISO system.

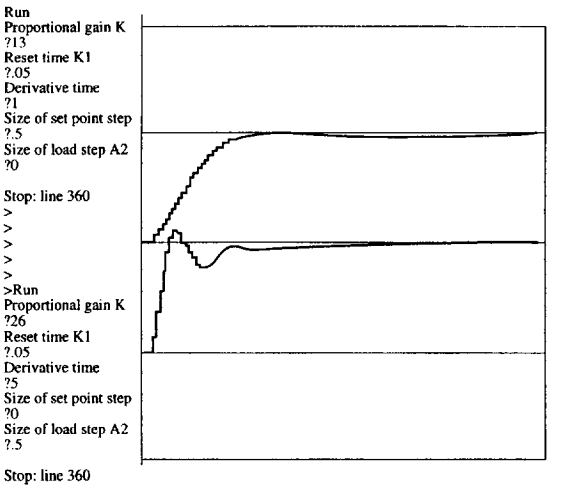

Fig. 29. PID control of SISO system.

The closed loop responses are given, see Figs. 27–29, for two cases:

(i) a step change in set point maintaining load disturbances at zero,

(ii) a step change in load maintaining set point at zero.

In both cases the closed loop controller will endeavour to attain the desired set point value. The results of such closed loop simulation responses for P control are shown in Fig. 27, for PI control in Fig. 28 and for PID control in Fig. 29. P control is abandoned due to offset errors, PI control gives an overshooting response; PID control speeds up the response with acceptable over/undershoot.

The appealing feature with this control scheme is that only one flowmeter and one actuator are used.

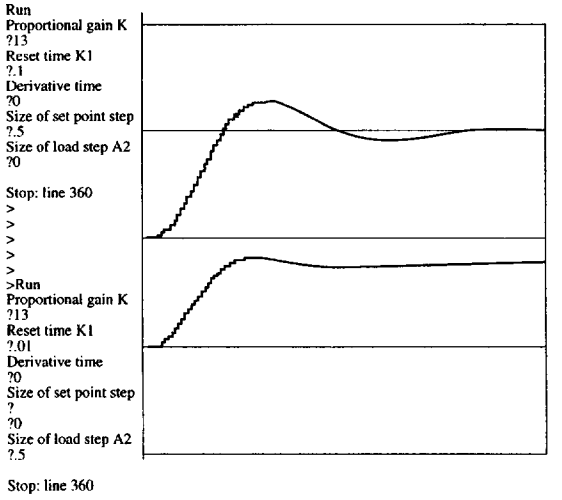

Fig. 28. PI control of SISO system.

11. MIMO closed loop controller scheme

In the case of MIMO, the experimental fluidized bed is automated by means of two control valves on the primary and secondary air stream, to regulate the mass flow rate and velocity, respectively in the conveyor.

The general block diagram of the closed loop system under development is given in Fig. 30. It is divided into:

- the measuring system
- the plant (dust feeder, conveyor)
- the interface control elements (valve) and
- the controller.

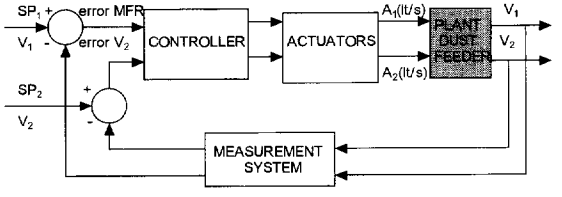

Fig. 30. Block diagram of the closed loop control scheme of the fluidized bed system.

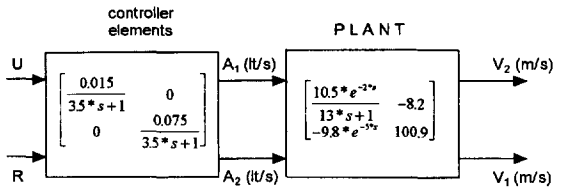

Fig. 31. Block diagram of MIMO open loop system.

Traditional and modern computer control model design techniques and simulation results are used [26]. There is no doubt that the SISO control scheme is adequate for the plasma spraying operating conditions but a multivariable control scheme would give better regulation of V_1 and V_2. Such a MIMO control scheme can satisfy the general case of a variety of particulate matter flowing through different pipe diameters.

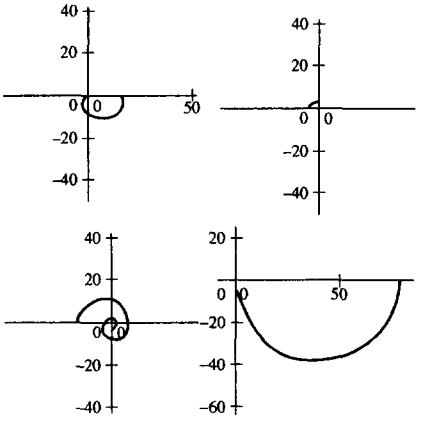

Fig. 32. Nyquist plots of open loop MIMO system.

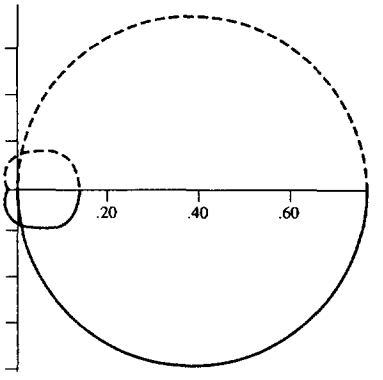

Fig. 33. Characteristic locus of open loop MIMO system.

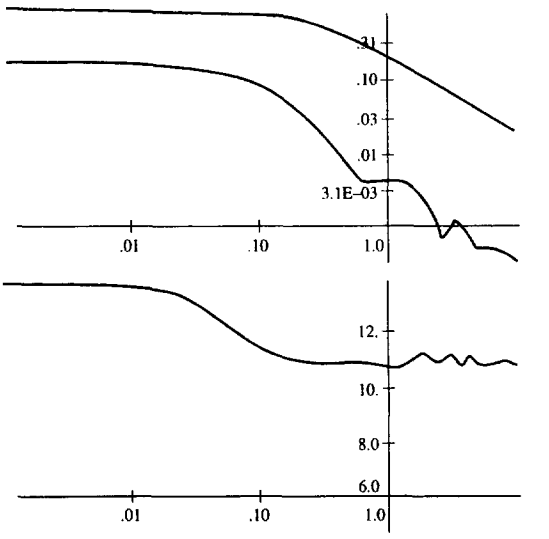

Fig. 34. Moduli and misalignment angles of open loop MIMO system.

The open loop MIMO transfer function is shown in Fig. 31. The plant transfer function matrix has $G_{11}(s)$ predominantly second order, $G_{21}(s)$ pure time delay, while $G_{12}(s)$ and $G_{22}(s)$ have a first order behavior. The dominant delay term of $G_{12}(s)$ cycles at the origin with increasing frequency.

It can be seen that the eigenvalues are not easy to calculate and simulation results are given by the UMIST CAIAD Computer-Aided Control Design software package on a PDP-11 platform. The process

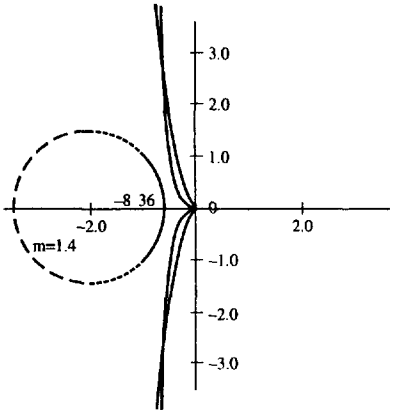

Fig. 35. PI controlled system characteristic locus and M circles for tuned MIMO.

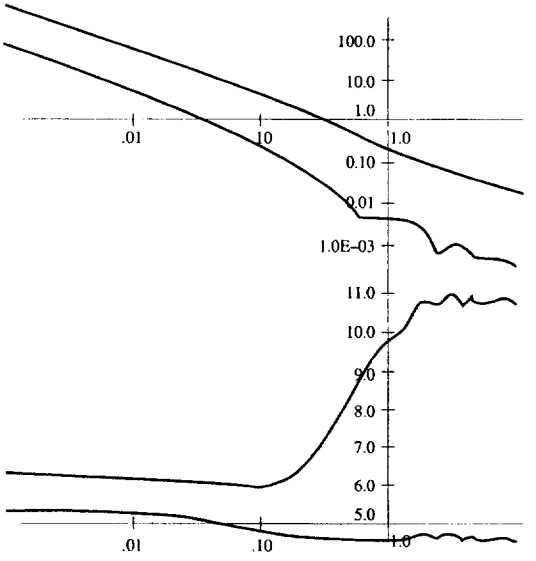

Fig. 36. Moduli and misalignment angles for tuned MIMO system.

dynamics are loaded into the computer and the more appropriate characteristic locus design method is initiated. Figure 32 shows the combined valves and plant open loop Nyquist plots of each matrix element.

The open loop characteristic locus of functions $g_1(s)$ and $g_2(s)$ are shown in Fig. 33, emphasizing the open loop stable nature of the system, i.e. no unstable open loops since the characteristic locus encircles the origin in an anticlockwise sense, More

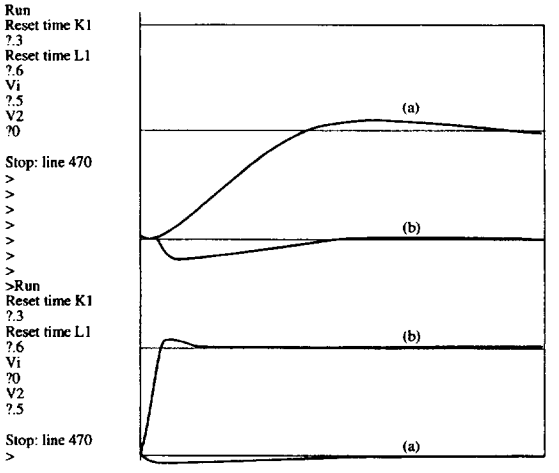

Fig. 37. Closed loop response of tuned MIMO control system controller.

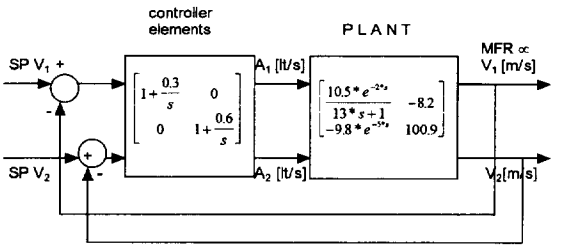

Fig. 38. Block diagram of MIMO closed loop system.

information is gained by looking at the Bode plots in Fig. 34, where at low frequencies the moduli are similar and the misalignment angles are relatively small. This indicates that the interaction is small and that the controller design can proceed without the use of a pre-compensator.

In order to achieve good steady state accuracy a PI type controller is applied and the results are given in Figs. 35 and 36. The closed loop response for the tuned MIMO control system is shown in Fig. 37, while the final MIMO control scheme is in Fig. 38. The resulting performance with tuned MIMO PI controller exhibits further optimized performance.

12. Conclusions

A controller (for both SISO and MIMO modeling approaches) for a dust feeder of a fluidized bed rig has been proved feasible; the system was identified and the controller design and stability investigated, for both the open and closed loop controller configuration. The intrinsic physical complexity of the process flow itself lies in the fact that its parameters are susceptible to changes, i.e the powder flow is not homogeneous, but consists of concentrations and rarefications of particles.

It is suggested that dust feeder design is the most interesting part in fluidized bed engineering. Further work should be done on the economics of the air and electrical power consumption in the fluidized bed.

Appendix A. Vocabulary

MFR = Mass Flow Rate
rms = Root Mean Square

SISO = Single Input – Single Output
MIMO = Multiple Input – Multiple Output
DDC = Direct Digital Control

References

[1] J.F. Davidson and D. Harrison, "*Fluidised Particles*", Cambridge University Press, Cambridge, 1963.

[2] G.E. Klinzing, "*Gas–Solid Transport*", McGraw-Hill, New York, 1981.

[3] M.S. Beck, "Selected papers for M.Sc. Course in Control Eng.", School of Control Eng., Bradford University, Bradford, 1978.

[4] R.F. Smart and J.A. Catherall, "*Plasma Spraying*", Mills & Boon, 1974.

[5] M.S. Beck and Wainwright, "Current Industrial Methods of Solid Flow, Detection and Measurement", *Int. Conf. of Powder Tech.*, Chicago, May, 1968.

[6] F.J. Atkins, "The Factors Affecting the Plasma Spraying Efficiency of Powders", *2nd Metal Spraying & Plastic Coating Conference*, Institute of Welding, London, 1967.

[7] D.E. Stock, "Measurements in Polyphase Flows", *American Soc. of Mech. Eng.*, California, 10–15 Dec 1978.

[8] Center for Professional Advacement, "Baghouse Dust Collection Systems", Notes of three day course, Amsterdam, 1995.

[9] J.S. Bendat and A.C. Piersol, "*Measurement and Analysis of Random Data*", John Wiley & Sons, New York, 1966.

[10] D.E. Ventzas, "A Microcomputer-based Cross-correlator for Fluid Flow Measurement", M.Sc. thesis, University of Bradford, Bradford, 1980.

[11] D.E. Ventzas, "An Instrumentation Indudstrial Correlator", *IASTED Int. Symp. of Applied Informatics*, Inssbruck, 18–20 Feb 1986.

[12] A.W. Bright, R.P. Corbett and J.F. Hughes, "*Electrostatics*", Engineering Design Guides, Oxford University Press, Oxford, 1978.

[13] M.E. Shackelton, "Electrodynamic Transducer for Gas–Solid Flow Measurement", M. Phil. thesis, Bradford University, 1982.

[14] A.D. Moore, "*Electrostatics and Applications*", Wiley Interscience, New York, 1973.

[15] M.R. Baum, B.N. Cole and F.R. Mobbs, "An Investigation of Electrostatic Charging Effects in High Speed Gas–Solid Pipe Flows", *Proc. Am. Ins. Mech. Eng*, paper 10, 1969.

[16] D. Geldhart and M. Haesebrouch, "Studies on the Intermitten Discharge of Coarse Solids from Fluidized Beds", *Trans. Chem. Eng.*, 1983.

[17] M.S. Beck and J.H. Hobson, "*Electrostatic Charge Measurement of Particulate Materials Being Transported at High Velocities — Explosion Risk Meter for Pneumatic Conveyors*", 1979.

[18] P.W. King, "Mass Flow Measurement of Conveyed Solids by Monitoring of Intrinsic Electrostatic Noise Levels", *2nd Int. Conf. on Pneumatic Transport of Solids, BHRA*, Sept 1973.

[19] N.A. Anderson-Bryan, "Mixture and Mass Flow Measurement of Powdered Granular Materials", M.Sc. thesis, University of Bradford, 1978.

[20] D.E. Ventzas, "Mathematical Modeling in Powder Transportation", *Modeling, Simulation & Control, B, AMSE* **7** (1) (1986) 1–11.

[21] W.R. Harber, "How Do Solid Surfaces Become Charged?" *Static Electrification Conf.*, Inst. Physics & Physical Soc., Series no. 4, 1967.

[22] Donaldson Co., "Standard Opereating Procedure of Donaldson Dust-Feeder", Research Division, project no: 1-91111B.

[23] Institute of Metal Sprayers, "*Directory of Metal Sprayers*", Ward Street, Walsall.

[24] Cohen and Coon, *Trans. ASME* (1953) **75**, 827.

[25] D.E. Ventzas, "Control Systems Theory and Technology", (**I–IV**), (in Greek), TEI Lamia, Electronics Dept., Greece, 1995.

[26] R.S.A. Thiga and N.E. Cough, "CAIAD Users' Guide", Report R128, June 1974, 1st Revision October 1974.